

Magnetic and Microstructural Study of Ferromagnetic Shape Memory Alloys

Final report Belspo project Dr. Jiangbo LU at EMAT, University of Antwerp, 15/11/2010 - 15/5/2012

Summary

The main topic of research of Dr. LU concerned the magnetic and microstructural study of Co-Ni-Al alloys using various transmission electron microscopy (TEM) techniques. Conventional TEM was performed to investigate the microstructures of two kinds of $\text{Co}_{38}\text{Ni}_{33}\text{Al}_{29}$ ferromagnetic shape memory alloys obtained from the Institute of Physics at the Academy of Prague. In the Bg190 sample which was fastest grown with the shortest annealing time, dendritic shaped γ' precipitates were observed in a martensite matrix with a precipitate-austenite-martensite sandwich structure at the precipitate-matrix interface. The formation of the sandwich structure can be explained by the presence of a Co-depleted and Al-enriched chemical gradient zone and the strong martensitic start temperature dependency on element composition. The orientation relationship between residual austenite and precipitate fits the Kurdjumov-Sachs orientation relationship. In the BM2 sample which was slower grown and annealed for a longer time, besides the dendritic shaped γ' precipitates, the faceted micron-sized precipitates without, or with one or three $\{111\}_p$ twin planes were observed in the austenite matrix. These precipitates with the twinning structure have a specific orientation distribution due to the existence of the $\{111\}_p$ twin plus the Kurdjumov-Sachs orientation relationship between precipitates and matrix. No chemical gradient zone across the interface between the precipitates and the austenite matrix was observed. The 3D morphologies of the precipitates were studied with Slice-and-View (FIB/SEM) while the magnetic domain structures of precipitates and matrix were studied by Lorentz microscopy. The latter was the first time at EMAT to apply the new Titan microscope for Lorentz microscopy.

Next to the originally planned work on $\text{Co}_{38}\text{Ni}_{33}\text{Al}_{29}$ Dr. Lu also worked on strain glass systems based on Ni-Ti and Ti-Pd-Cr alloys using HRSTEM aberration corrected HR(S)TEM. He further also supported the PhD work of Hui SHI on large hysteresis Ti-Ni-Nb shape memory material and joined a project on zeolite microcrystals. Dr. Lu will stay at EMAT till September 2013 to continue his research on these various topics and finalize several publications.

2. Material and Methods

Bulk single crystal $\text{Co}_{38}\text{Ni}_{33}\text{Al}_{29}$ samples were prepared by the Bridgman method. The different preparation and annealing conditions applied in the present work to the as-cast single crystals to control M_s , M_f , etc. are listed in Table 1. The martensitic transformation temperatures were determined by differential scanning calorimetry

(DSC). One main important difference between the effects of the crystal growth rate and subsequent thermal treatment is that for Bg190 the resulting M_s is around room temperature while for BM2 it is far below room temperature, yielding secondary phase precipitates embedded in martensite and austenite matrix, respectively. In what follows it will also become clear that the microstructure as such is substantially different.

Table 1: Pulling rates, annealing temperature and time, and temperature of martensitic start transformation for the studied materials.

	Pulling rate [$\mu\text{m}\cdot\text{s}^{-1}$]	Annealing temperature and time [K/h], followed by water quenching	M_s [K]
Bg190	28.8	1623/1	> 298
BM2	7.7	1373/72	< 173

Conventional TEM samples were prepared by twin-jet electropolishing in a 20% sulfuric acid and 80% methanol electrolyte at 258K. In order to enable an adequate study of the matrix-precipitate interface, an FEI Nova 200 Nanolab Dual Beam SEM/FIB system was applied to get cross-sections from the place of interest. A standard ion column is installed which allows Ga^+ milling at 5-30KV. The Slice-and-View study of the 3D morphologies of the precipitates was carried out with the same equipment. Conventional TEM was carried out on a LaB_6 Philips CM20, and the high-resolution and analytical STEM-EDX analysis was performed on a FEG FEI Tecnai G2, both microscopes were operated at 200KV. The Lorentz study was carried out on an FEI aberration-corrected monochromated Titan operating at 300KV.

3. Microstructural study

Fig. 1(a) shows a SEM image of the bulk **Bg190** sample, which reveals some detail of the morphology of the sample with an dendritic structure yielding micron-sized precipitates embedded in a martensitic matrix at room temperature, which is consistent with M_s being around room temperature as listed in Table 1. In this sample these large precipitates or the martensite-precipitate interfaces do not reveal any particular crystallographic shapes. In order to investigate the details of the martensite-precipitate interface a FIB TEM lamella was prepared from the position indicated by the white bar.

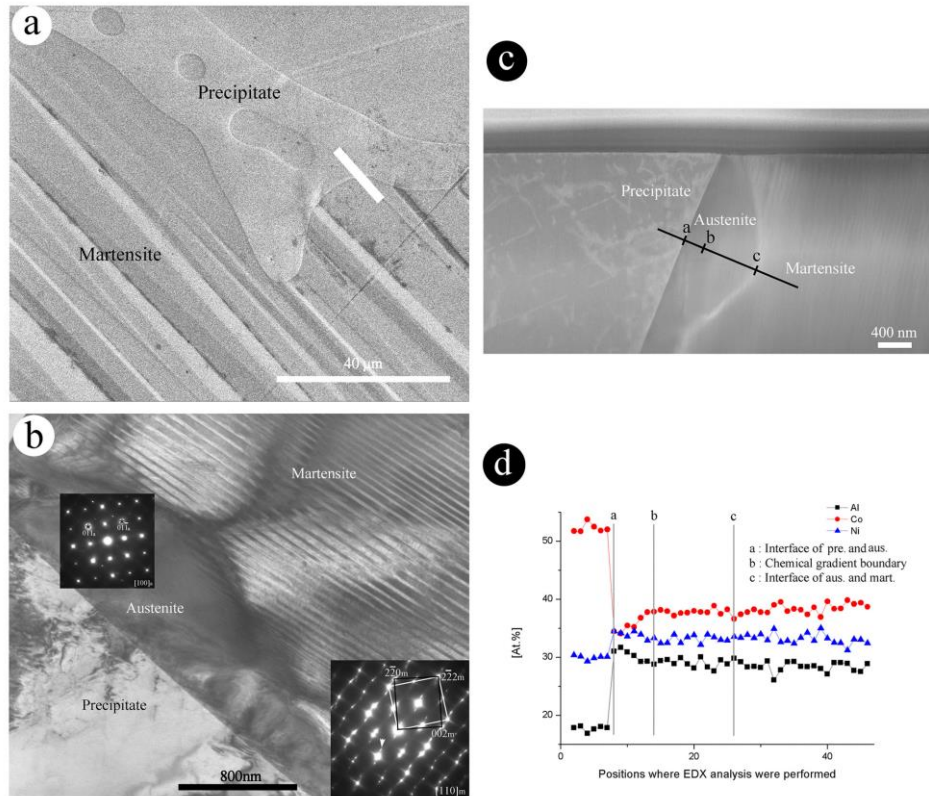


Fig. 1 (a) Typical SEM image of the microstructure of the bulk Bg190 sample, (b) BF image of FIB cross-section sample taken along $[100]_a$ zone axis of residual austenite phase, (c) STEM image of the FIB lamella, (d) Concentration profiles of alloy elements across the precipitate-austenite-martensite region shown in (c) using a STEM-EDX line scan method.

Fig. 1(b) shows the bright field (BF) image of the FIB lamella taken along the $[100]_a$ zone axis of the austenite (the subscript “a” and “m” further-on in the text denote austenitic and martensitic structure, resp.). The right upper part exhibits the typical twinning structure of the martensitic phase. The electron diffraction pattern of the twin lamellae along the $[110]_m$ zone axis is shown at the right lower corner and consists of two sets of overlapping diffraction patterns. Each set of the pattern can be indexed by the typical $L1_0$ tetragonal martensitic structure with $a=b=0.385\text{nm}$, $c=0.314\text{nm}$. The two sets of patterns share the spots along the $\mathbf{g}_{[1-11]_m}$ direction, i.e. the diffraction spots along the $\mathbf{g}_{[1-11]_m}$ direction are unsplit, which indicates the twin plane (martensite plate boundaries) are the $(1-11)_{L1_0}$ planes. The small diffraction spots indicated by the white arrow might originate from surface martensite due to Ga^+ ion irradiation during FIB sample preparation. The middle part of Fig. 1(b) reveals the morphology of the austenitic phase. The corresponding electron diffraction pattern taken along the $[100]_a$ zone axis is shown at its upper part, and can be indexed by the B2 cubic structure with $a=0.285\text{nm}$. Comparing the diffraction patterns of the austenite and martensite in Fig. 1(b), the expected orientation relationship $[100]_a \parallel [110]_m$, and $(01-1)_a \parallel (1-11)_m$ accompanying the martensitic phase transition and arising from a simple tetragonal distortion of the cubic cell can be confirmed. The left lower part of Fig. 1(b) reveals the morphology of the precipitate with a slightly bend

interface with the sandwiched austenite region.

Fig. 1(c) shows a STEM image across the region of the precipitate-austenite-martensite sandwich structure. The black line shows the trace along which a STEM-EDX line scan analysis was performed. The characters *a*, *b* and *c* indicate the interface of precipitate and austenite, the boundary of the chemical gradient zone in the austenite (see below) and the interface of the austenite and martensite, resp.. Fig. 1(d) shows the concentration profiles of three elements across the sandwich structure. From these profiles we can clearly observe the Co depletion and Al enrichment in the *a-b* gradient zone compared with the *b-c* zone (although the position of “*b*” remains a bit arbitrary). For the present region, the width of this chemical gradient zone is around 200 nm, while other gradient regions in the sample were found to be between tens of nm to a maximum of 250nm. It is also important to mention that the size of the austenite, which is in the range of tens of nm to several micrometers, depends on the size and morphology of the precipitate. The quantified mean EDX values of the different regions across the precipitate-austenite-martensite sandwich structure are shown in Table 2. The data quantitatively show the presence of the Co depletion and Al enrichment in the *a-b* chemical gradient region, as well as a small composition difference between the austenite *b-c* and martensite regions. In addition, the concentrations of Ni in the austenite and martensite are almost the same, about 3 at.% higher than in precipitate.

Table 2: The average element concentrations of different regions in Fig .1(c) including statistical standard error values.

Positions	Co [at. %]	Ni [at. %]	Al [at. %]
Precipitate	52.28 ± 0.32	29.98 ± 0.15	17.74 ± 0.18
Region <i>a-b</i> austenite	35.96 ± 0.58	33.85 ± 0.23	30.18 ± 0.41
Region <i>b-c</i> austenite	37.89 ± 0.14	33.10 ± 0.20	29.00 ± 0.23
Region martensite	38.33 ± 0.19	33.21 ± 0.19	28.44 ± 0.19
Area inside the precipitate (Fig. 3)	36.61 ± 0.42	32.94 ± 0.35	30.43 ± 0.27

In order to interpret the formation of the precipitate-austenite-martensite sandwich structure, the positions representing the element concentrations of different regions shown in Table 2 have been added to the Co-Ni-Al ternary phase diagram in Fig. 2 including the composition dependency of M_s . The dashed lines show the iso-contour temperatures of M_s , which indicate that M_s decreases with an increase of both Co and Al contents. For the martensite matrix, the composition indicates an M_s slightly below room temperature, which might indicate a certain systematic shift of the present measurements or of the phase diagram, probably due to the well-known very high sensitivity of M_s to composition in SMA. From the relative measures, however, it is clear that M_s (region *a-b*) < M_s (region *b-c*) < M_s (region martensite) where especially the two extreme cases properly explain the formation of the precipitate-austenite-martensite sandwich structure. This means that the presence of the Co depleted and Al enriched chemical gradient zone and the composition

difference between austenite and martensite result in a structure separation due to the strong dependency of M_s on alloy composition. Moreover, due to the orientation of the M_s iso-contour lines the changes in Al content play the most important role in this particular alloy. A similar phenomenon was reported in Ni-Ti shape memory micro-wire where the concentration gradient of the alloying elements stemming from the oxidation of the surface results in the formation of a martensite-austenite core-shell structure for the entire micro-wire.

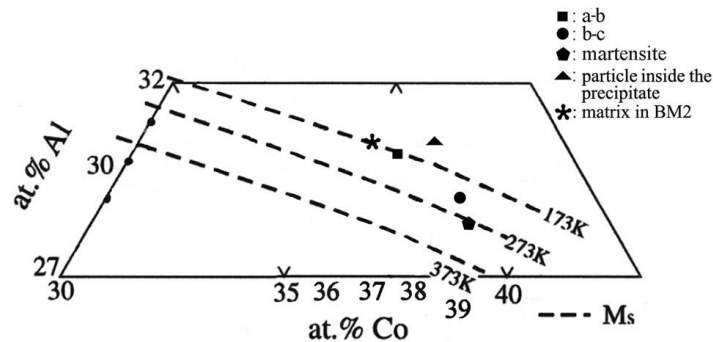


Fig. 2 Observed concentrations in the sandwich structure in view of composition dependency of the martensitic start transformation temperature M_s in the Co-Ni-Al ternary system.

However, the small difference in composition between the martensite and region *b-c* of the austenite does not explain the particular shape of the austenite region in this area. On the other hand, from the relative lattice orientation between austenite and martensite observed in Fig. (1), it is clear that the expected crystallography of the cubic-to-tetragonal transformation has been retained and the system will have to compete between the volume energy of both phases, governed by the concentration, and the surface energy at the habit plane induced by the transformation strain. This has probably resulted in the particular hat-shape of the austenite-martensite interface in Fig. 1(b), yielding an austenite region slightly extending into an area with a higher Co and lower Al content.

Fig. 3(a) shows a SEM image of another area of the Bg190 material. Besides the martensite variants recognized in the matrix, we can clearly observe a complicated dendritic structure of the precipitate with the inclusion of some round and rod-like areas. In order to investigate the crystal structure and chemical information of the internal areas, a FIB cross-section lamella from the position indicated by the white bar was prepared. Fig. 3(b) shows the BF image of this FIB lamella, revealing a knife-shaped zone with some internal microstructure surrounded by the precipitate. The majority of the diffraction patterns from this knife-shaped zone, as well as those from other internal areas in these dendritic structures, can be indexed by the B2 cubic austenitic phase. The fine twinning contrast in the center of the present austenite region stems from a small martensitic layer which is seen in overlap with the austenite.

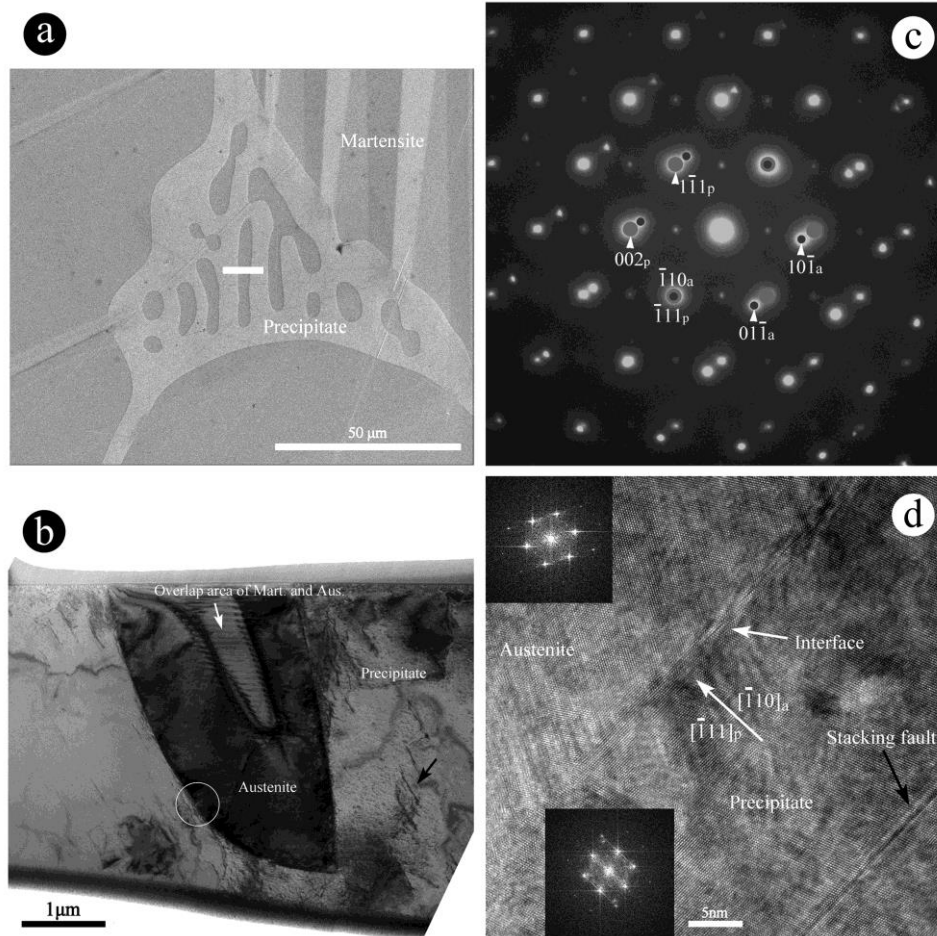


Fig. 3 (a) SEM image of the bulk Bg190 material showing the dendritic morphology of a γ' -precipitate (white bar indicates the position where the TEM lamella was prepared by FIB), (b) BF TEM image of the FIB lamella, (c) Electron diffraction pattern taken from the area indicated by the white circle in (b) ($[111]_a / [110]_p$), (d) HRTEM image of the interface of the precipitate and austenite corresponding to (c) including some FFT patterns.

The selected area electron diffraction (SAED) pattern from the interface of the austenite and precipitate indicated by the white circle is shown in Fig. 3(c) and consists of two sets of diffraction patterns. One of them can be indexed by the austenite crystal structure along the $[111]_a$ zone axis while the other one by the precipitate $L1_2$ crystal structure with $a = 0.351\text{nm}$ along the $[110]_p$ zone axis as indicated by white arrows (the subscript “p” denotes precipitate structure), resp. It is clear that the diffraction spots along the $\mathbf{g}_{[-110]_a}$ (or $\mathbf{g}_{[-111]_p}$) direction occur without splitting. Thus, the following orientation relationship between the austenite and precipitate was found: $[111]_a // [110]_p$, $(-110)_a // (-111)_p$, which belongs to the Kurdjumov-Sachs relationship. Fig. 3(d) shows the HRTEM image of the interface corresponding to Fig. 3(c). Insets show the FFT images of the corresponding regions.

In order to investigate the chemical information of the austenitic phase, again quantitative EDX analysis was performed. The average element concentrations are shown in the last line of Table 2. The position indicated by a triangle corresponding to the composition is shown in Fig. 2, from which it is clear that the M_s of this area is far

below room temperature explaining the austenitic phase formation inside the precipitate. The small martensite area in the center of the zone of Fig. 3b again indicates the end of the competition between the volume and surface energy terms. The black arrow in the lower right corner of Fig. 3d indicates the presence of a stacking fault in the precipitate.

In some other samples of this same series, treated in slightly different ways, precipitates as found in this Bg190 sample but completely embedded in austenite matrix were found. Again some Co depletion and Al enrichment was observed in the matrix near to the precipitate, but since the matrix is already in the austenite phase, no structural effect is induced by this concentration gradient.

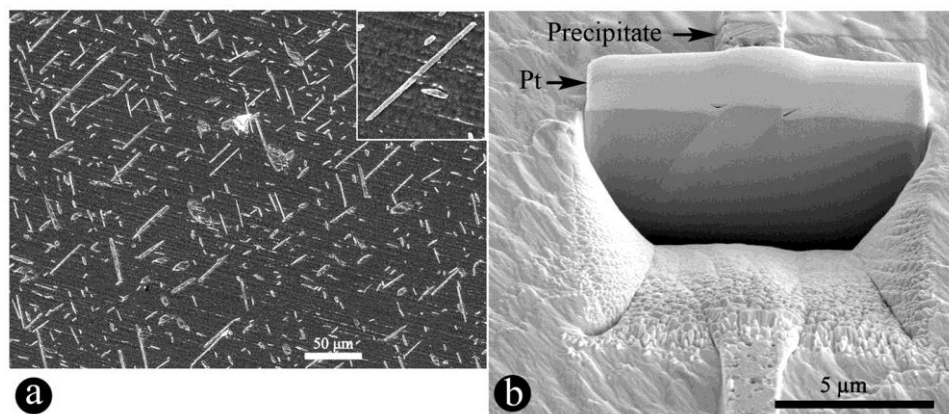


Fig. 4 (a) SEM image of the bulk BM2 material showing the homogeneous distribution and surface cross-section morphologies (needles and ellipses) of the γ' -precipitates at low magnification, (b) High magnification of a FIB cross-section cut from the middle of a single precipitate revealing a central interface.

For comparison we prepared the **BM2** sample as shown in Table 1 with a pulling rate of $7.7\mu\text{m}\cdot\text{s}^{-1}$ and annealed at 1373K for 72 hours, yielding an M_s far below room temperature. In this sample, besides the complicate dendritic γ' $L1_2$ precipitates similar to what we observed in Bg190, many micron-sized precipitates were found (sometimes up to 50 micron long) in the austenite matrix as seen from the SEM image in Fig. 4(a) and, as expected, no martensite traces in the matrix. The precipitates are somewhat smaller than the dendritic precipitate and they have a clear crystallographic shape, with many showing up as needles and some as ellipses on the surface of the SEM sample. A FIB cross-sectional cut of a single precipitate showing up on the surface as a needle was made and shown in Fig. 4(b). From this cut it is clear that the precipitates are formed as elongated flattened sheets with one long axis and an apparent central interface.

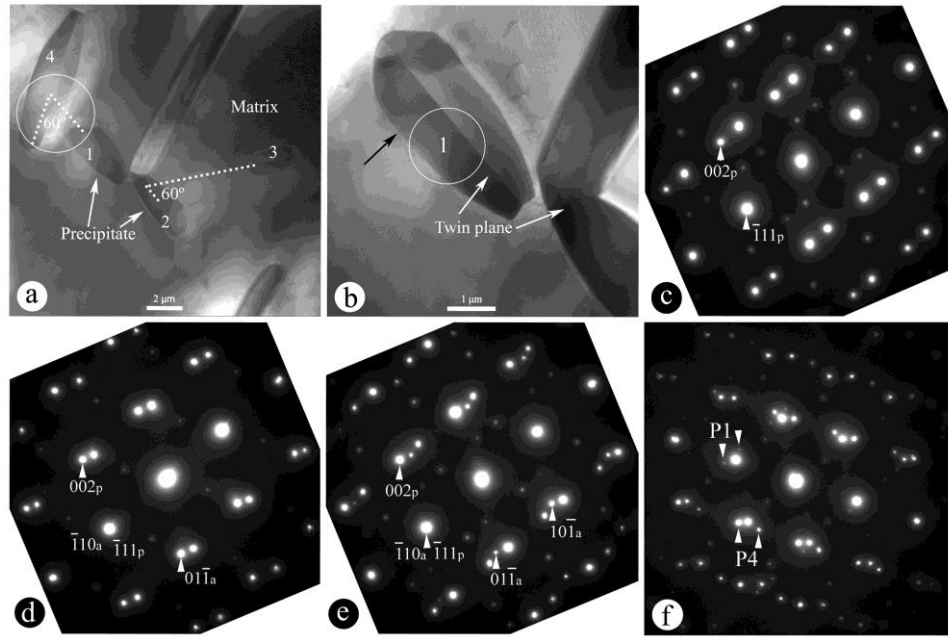


Fig. 5 (a) BF image of several γ' precipitates in BM2 material taken along the $[110]_p$ of precipitate-1 (= $[111]_a$), (b) BF image of precipitate-1 at higher magnification (several degree off to the $[110]_p$), (c) $[110]_p$ SAED of precipitate-1 from the twinning region, (d) $[110]_p$ SAED of precipitate-1 from the interface of precipitate-1 and matrix showing the K-S orientation relationship, (e) $[110]_p$ SAED of precipitate-1 from the region indicated by the white circle in (b), (f) $[110]_p$ SAED of precipitate-1 from the region indicated by the white circle in (a) (the major spots from the $[111]_a$ matrix).

TEM SAED again reveals these precipitates have the γ' $L1_2$ structure. In the BF image of Fig. 5(a) the B2 matrix is viewed along a $[111]_a$ zone axis and six relatively small precipitates are observed of which four are labeled in order to illustrate their relative orientation relationships. Typical dimensions for these precipitates are two or three microns in thickness and a few microns in length (i.e., on the small end of the distribution scale when compared with the SEM image). Fig. 5(b) shows the BF image of precipitate-1 at a higher magnification (several degree off the $[110]_p$ zone axis to enhance twin contrast) revealing a single $(-111)_p$ twin plane along the central axis. Fig. 5(c) shows the corresponding SAED pattern of the twinning structure in Fig. 5(b). Fig. 5(d) shows the SAED pattern taken along $[110]_p$ zone axis of precipitate-1 from its interface with the austenite matrix as indicated by the black arrow in Fig. 5(b). The latter confirms the Kurdjumov-Sachs orientation relationship between the two structures as in Fig. 3(c), i.e., $[111]_a//[110]_p$, $(-110)_a//(-111)_p$. Fig. 5(e) shows the SAED pattern which consists of the diffraction patterns shown in Fig. 5(c) and Fig. 5(d) from the region indicated by the white circle in Fig. 5(b), i.e., containing the twinned precipitate as well as the austenite matrix. Fig. 5(f) shows the diffraction pattern taken from the area as indicated by the white circle in Fig. 5(a) containing the twinned precipitate-1, twinned precipitate-4 and austenite matrix. The white arrows in Fig. 5(f) indicate the diffraction spots from the twinning structures of both precipitates. From Fig. 5(f) we can measure an angle of 60° between the twin plane of precipitate-1 and -4, confirming the measurement in Fig. 5(a). Twin plane orientation

relationships between precipitates-1, -2 and -3 were also examined from their diffraction patterns relative to the diffraction pattern of the matrix, confirming the correspondence of the $\{111\}_p$ twin planes with the corresponding $\{110\}_a$ austenite planes as well as the full KS orientation relationship. The long unlabeled precipitate also observed in Fig. 5(a) seems to have its twin plane inclined to the viewing direction. From the relative orientation relationships, it can be concluded that the shaped precipitates in the BM2 sample have a specific orientation distribution due to the existence of the $\{111\}_p$ twin planes inside the precipitates plus the Kurdjumov-Sachs orientation relationship between precipitates and matrix.

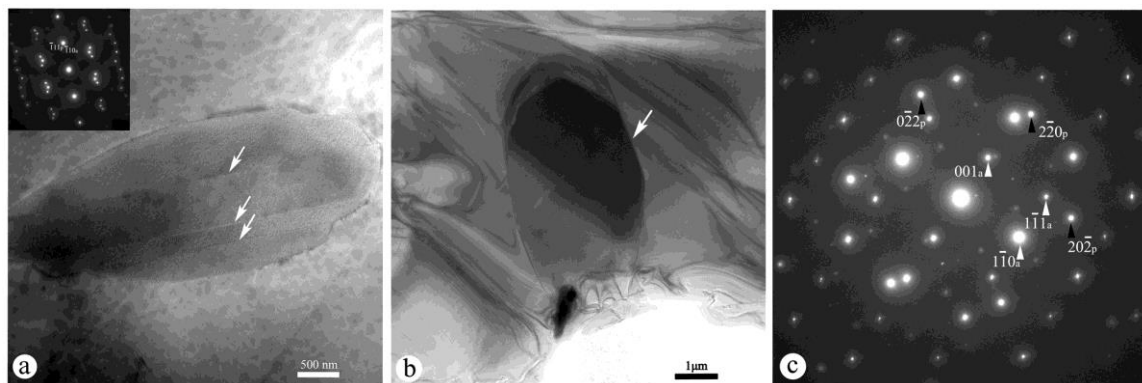


Fig. 6 (a) BF image showing three $\{111\}_p$ twin planes in a γ' precipitate in BM2 material observed along the $[110]_p$ zone axis of the precipitate (inset shows the corresponding SAED), (b) Shows the BF image of a precipitate taken along its $[111]_p$ zone axis ($= [110]_a$), (c) Corresponding SAED taken at white arrow in (b), the spots indicated by white arrows in (c) are from matrix, the ones indicated by black arrows are from precipitate (weak spots around the main reflection spots are due to double diffraction).

It also seems that the external shape of the precipitates is connected to the occurrence of the internal twin plane. The observed cross-sections of the precipitates in the TEM BF images of Fig. 5(a,b) reveal needle shapes with large edges parallel with the internal central twin planes, i.e. close-packed $\{111\}_p$ habit planes. At the corners various smaller edges are found parallel to other small index crystallographic planes (e.g., $\{200\}_p$ or $\{110\}_p$). Although most γ' precipitates contain only one single twin Fig. 6(a) shows the BF image of a precipitate containing three parallel $\{111\}_p$ twin planes taken along the $[110]_p$ zone axis. The corresponding SAED pattern taken from the whole area, i.e. including the surrounding matrix, is shown in the upper left corner. Fig. 6(b) shows a BF image of a precipitate taken perpendicular to the twin plane revealing a close to elliptic plan-view shape of the precipitate. The long axis of this elliptic shape is along the $[-111]_a$ direction of matrix. This view confirms the few elliptic shapes observed in the SEM image of Fig. 4 and already indicates that a twinned precipitate will grow faster along the plane of the twin than perpendicular to the twin. The observation of a needle shape for these precipitates can thus be correlated with the occurrence of this central twin plane resulting in surface facets of different growth speed essentially yielding two-dimensional crystals. Indeed, a single

(111)_{fcc} twin plane yields dense and slow growing (111)_{fcc} surface planes on both sides and parallel to this central twin plane while a re-entrant groove at which preferential lateral growth occurs is present on three sides of the twin plane (see, e.g., right side of precipitate-1 in Fig. 5(b)). For free growing crystals this will result in perfect triangular or hexagonal crystals, depending on the actual number of parallel twins. However, in the present case, with surrounding crystalline matrix and a K-S relationship, flat faceted sheet-like precipitates with different aspect-ratios will be formed and the observed needles can thus be interpreted as (electro)polished cross-sections of these sheets, the latter having a diameter at least twice as large (and often much more) than their height or thickness.

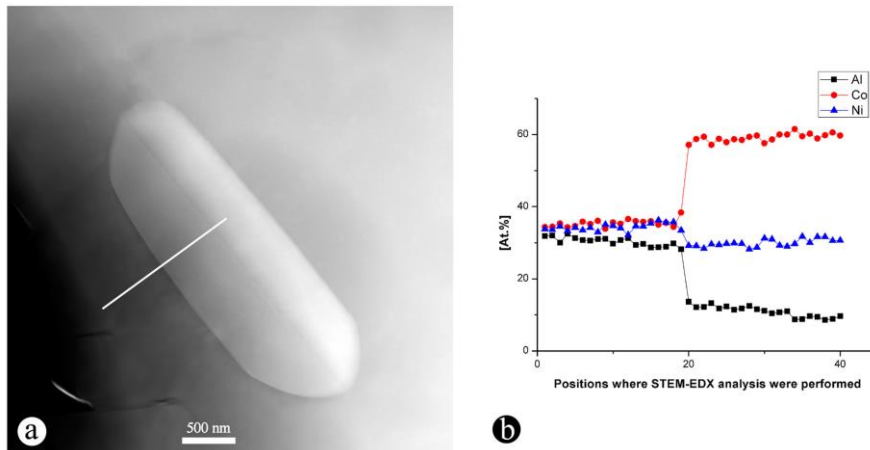


Fig. 7 (a) STEM image of a BM2 precipitate, (b) The concentration profiles of the three elements across the precipitate-austenite interface: no dip near the interface is observed.

Similar as for Bg190, we also carried out a STEM-EDX line scan analysis to investigate the chemical information across the interface between the precipitate and austenite: here, as seen in Fig. (7) and listed in Table 3, no chemical gradient zone in the austenitic phase was observed, so it can be concluded that the BM2 sample is prepared under full equilibrium conditions, in contrary to the Bg190 material, which is consistent with a much longer annealing time.

Table 3: Quantitative concentrations obtained from the element profiles in Fig. 7(b), including statistical standard error values.

	Co [at. %]	Ni [at. %]	Al [at. %]
Matrix	35.21±0.18	34.34±0.25	30.44±0.27
Precipitate	59.12±0.24	29.93±0.23	10.94±0.33

Comparing the data in Table 3 with the element concentrations in the Bg190 sample in Table 2, we can see that the amount of Co in the precipitates in the BM2 sample is higher than in the Bg190 sample and that the amount of Al is less than in the Bg190 sample. In the matrix of course the opposite tendency occurs which explains the austenite structure for the BM2 sample. Indeed, when the composition for the

BM2 matrix is added to Fig. 2 an M_s of 173K is found confirming the DSC measures listed in Table 1. A dendritic growth of the matrix and γ precipitate was observed in as-cast $\text{Co}_{38}\text{Ni}_{33}\text{Al}_{29}$ samples at any growth rate including $7.7 \mu\text{m.s}^{-1}$ (BM2) and $28.8 \mu\text{m.s}^{-1}$ (Bg190) using the Bridgman method. Apparently different subsequent annealing treatments in the present study yields different morphologies of precipitates with the most prominent changes being introduced by the BM2 treatment.

Under different circumstances apparently genuine rod- or needle-shaped precipitates have been reported in this system before. However, no $L1_2$ ordering was observed and no twinning inside the precipitates was concluded. In both cases the long axes of the rod was seen to grow in the $\langle 111 \rangle$ direction of the B2 matrix, following the direction of the lowest interface misfit, similar to the lens-shape of Ni_4Ti_3 precipitates playing an essential role in the functional behaviour of SMA alloys of the Ni-Ti system. In the latter case the change in interplanar spacing in the direction perpendicular to the central plane of the precipitate induces a strain gradient in the matrix hindering the growth of the precipitate in this direction.

The larger γ' $L1_2$ precipitates observed in the BM2 samples of the present work, however, do contain at least one plan-parallel internal twin plane. The reason that the twinned precipitates are only observed in the BM2 sample can be understood from energy competition between the formation of this internal defect and the surface energy at the precipitate/matrix interface. Indeed, by nucleating with an internal twin the precipitate can grow with large low energy close packed $\{111\}_p$ surface planes which also induce the least strain inside the matrix. The latter can be concluded from BF images as in Fig. 6(a) not showing any strain contrast but also from the typical K-S diffraction pattern in, e.g., Fig. 5(d) from which the lattice planes in the precipitate and matrix parallel to the interface are found to have the same interplanar spacing. As indicated above, resulting from the internal twin are re-entrant grooves at the edge of the precipitate promoting its growth along these edges. However, when the annealing temperature is increased as in sample Bg190 the advantage of having large low energy surface planes will be diminished by an increase of entropy and the gain of forming a twin plane at the nucleation of the precipitate (and increasing its total energy) will be minimized, eventually leading to single crystal precipitates without faceting, but with dislocations and stacking faults accommodating internal strain, as seen at the black arrow in Fig. 3(b).

Slice-and-View was carried out in order to study the 3D morphologies of the precipitates in the BM2 sample. Slice-and-View is a powerful method to study the 3D morphologies of the precipitates in alloys. In our experiment, ion beam worked at 30 kV, 9.5 nA and the electron beam worked at 5kV, 1.6nA. The thickness of the slice cut off is 100nm.

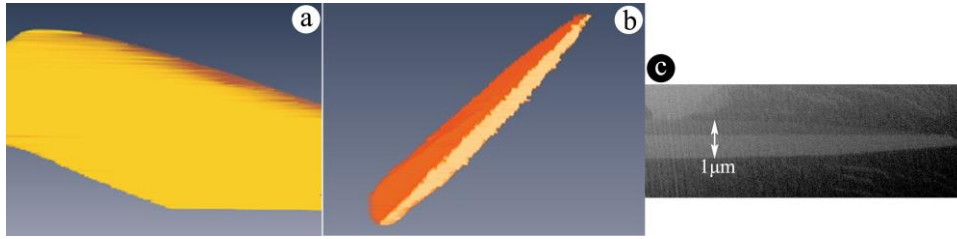


Fig. 8(a, b) show the reconstructed image of the 3D morphology of one precipitate with twinning plane inside and viewed along different directions. Fig. 8(c) shows one of the SEM images used for reconstruction, from which the twinning of the precipitate can be observed.

Fig. 8 (a, b) shows the constructed images of one precipitate with one twinning plane inside the precipitate viewed from different directions with Slice-and-View technique. Fig. 8(c) shows one of the cross-section SEM images of the precipitate used for reconstruction.

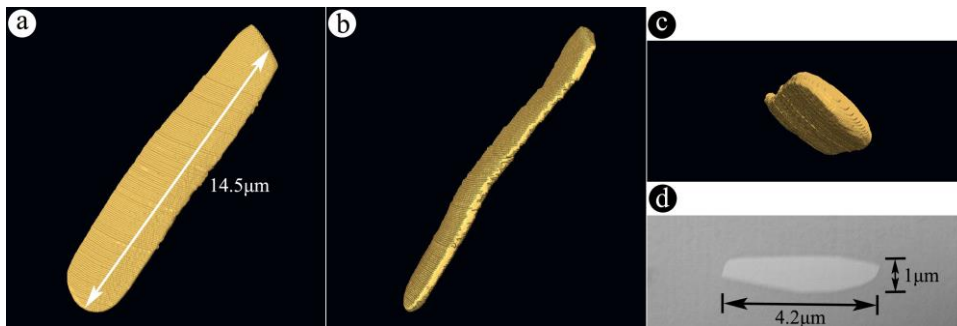


Fig. 9 (a-c) shows the reconstructed images of one precipitate without twinning viewed along different directions. Fig. 9(d) shows one of the SEM images used for the reconstruction.

Fig. 9 (a-c) shows the reconstructed images of one precipitate without twinning viewed along different directions. We can see the precipitate has a slab-like shape. The thickness is about 1 micron. Fig. 9(d) shows one of the cross section SEM images of the precipitate used for the 3D reconstruction, revealing the absence of the twinning inside the precipitate.

4. Study of the magnetic structure

In order to investigate the magnetic domain structures of the precipitates and matrix, Lorentz microscopy was performed. Fig. 10(a) shows the BF image of one precipitate without a twinning plane, the inset shows the correspondent diffraction pattern of the whole area. It was found that the precipitate lies along the $[-11-1]_p$ direction and the interface between precipitate and matrix is $\{-11-2\}_p$ as indicated by white arrows. Fig. 10(b-d) shows the Lorentz Fresnel image of the precipitate observed at over-focus, in-focus and under-focus conditions at room temperature, respectively. A closure domain can be observed inside the precipitate in Fig. 10(b, d). The white arrows indicate the domain walls. The reversal of the magnetic domain wall contrast can be observed, and the domain contrast is diminished at the in-focus

condition. Considering the crystallographic direction of the precipitate and the morphology of the domain structure, the easy axis of the precipitate can be determined to be $\langle 111 \rangle_p$. The black arrows in Fig. 10(d) indicate the magnetization directions in the closure domains.

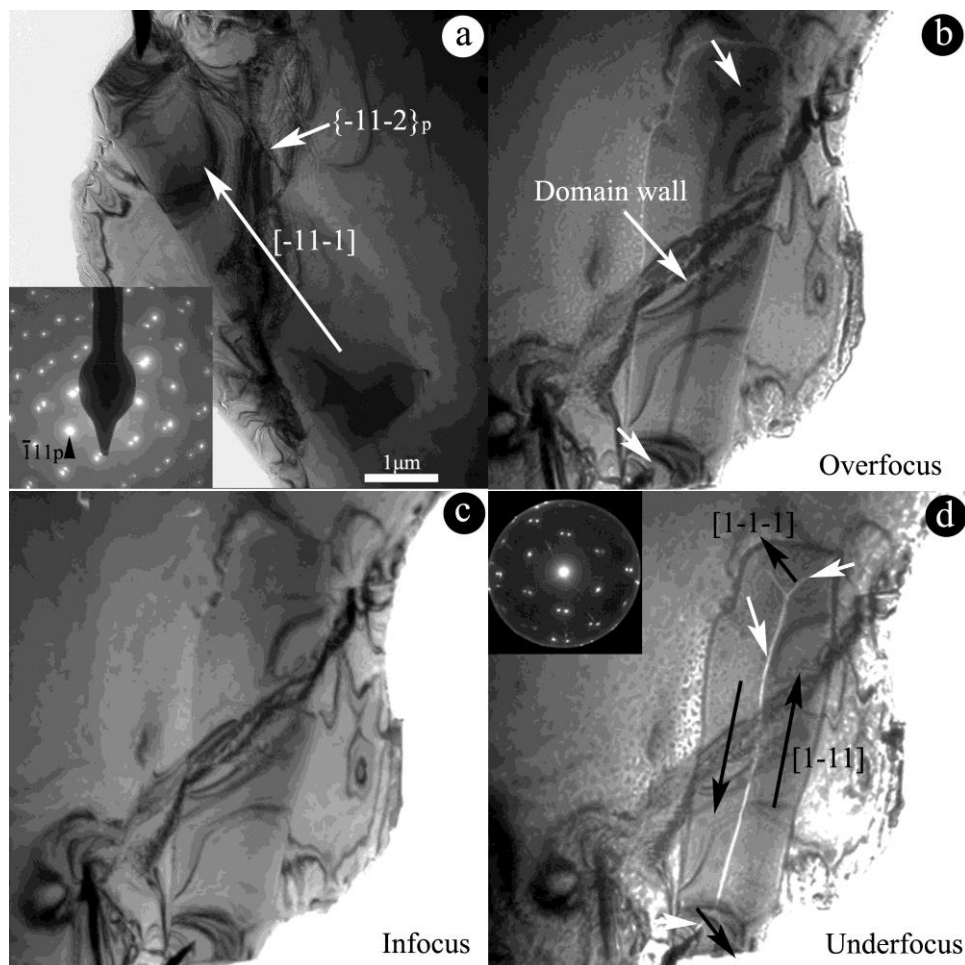


Fig. 10(a) shows the bright field image of one precipitate, the inset shows the selected area diffraction pattern of the area including the precipitate and matrix. Fig. 10(b-d) show the over-focus, in-focus and under-focus Fresnel image of the precipitate, respectively.

Fig. 11(a-d) shows a series of Fresnel images of the matrix obtained during an in situ cooling experiment. Fig. 11(a) shows the over-focus Fresnel image at room temperature. No magnetic domain contrast can be observed, which indicates the matrix is paramagnetic. The selected area diffraction pattern at the upper left side of Fig. 11(a) was obtained from the whole area. Fig. 11(b,c) shows the over-focus and under-focus Fresnel image of matrix at -100°C . The inverse of the magnetic domain wall contrast can be observed, from which it can be concluded that the straight black and dark lines are domain walls in the sample. Fig. 11(d) shows the over-focus image at -150°C . As we can see more magnetic domains appear when the sample is cooled down. According to the M_s of the BM2 sample in Table 1, the matrix should transform into martensite at -150°C . However, no martensitic transformation took place when we kept the sample at -150°C for half an hour or even further cooling to

-170°C. The reason can be the inhomogeneity of the element composition in the sample, which can strongly affect the local M_s transformation temperature or a thin foil effect hampering the structural transformation. Taking into account of the crystallography directions and the 180° walls, the magnetic easy axis of the matrix can be determined to be [001] or [111]. Fig. 11(e) shows the over-focus Fresnel image of another area of the matrix, as we can see the sample is austenite at the thinner area whereas the sample is martensite at the thicker area.

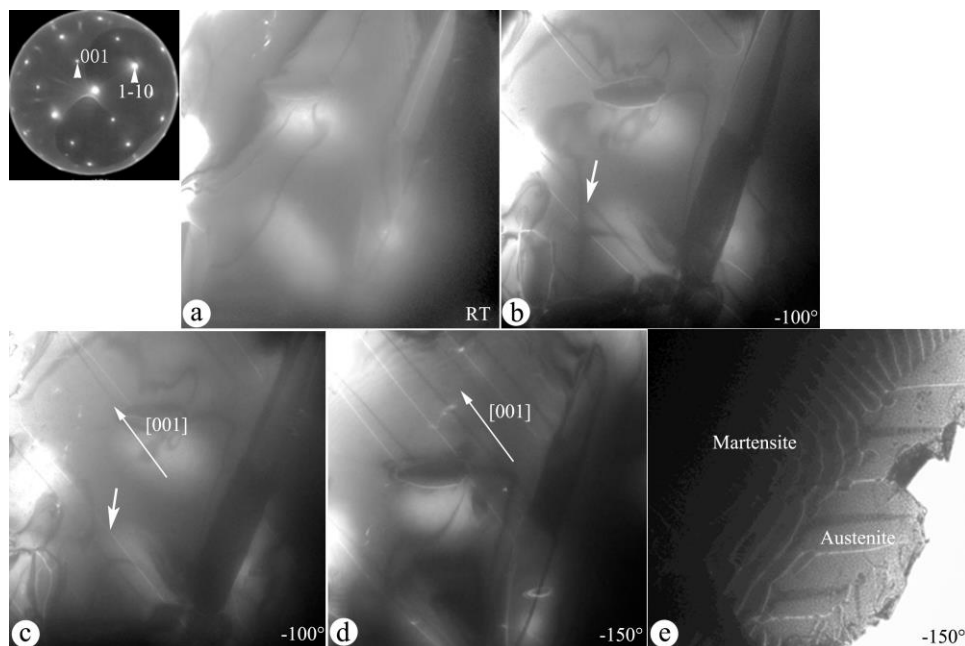


Fig. 11(a) shows the over-focus Fresnel image of the matrix at room temperature. (b, c) show the over-focus and under-focus Fresnel image of the same area at -100°C . (d) shows the over-focus image of the matrix at -150°C . (e) shows the over-focus image of the matrix from another area at -150°C , from which the coexistence of the martensite and austenite can be observed.

5. Conclusions

Transmission and scanning electron microscopy supported by analytical techniques were performed to investigate the microstructure, 3D morphologies of the precipitate and the magnetic domains of two kinds of $\text{Co}_{38}\text{Ni}_{33}\text{Al}_{29}$ ferromagnetic shape memory alloys, treated in different ways. The following conclusions are obtained:

- (1) In the Bg190 sample, grown with a pulling rate of $28.8 \mu\text{m}\cdot\text{s}^{-1}$ and annealed at 1623K for 1h, the matrix shows large martensite regions and γ' precipitates have a complicated dendritic structure with enclosed B2 austenite areas. Also, a precipitate-austenite-martensite sandwich structure with residual austenite of several hundred nanometers wide is formed due to the depletion of Co and enrichment of Al in the chemical gradient zone and the effect of the strong martensitic start temperature dependency of the element concentrations. The orientation relationship between residual austenite and precipitate fits the

Kurdjumov-Sachs orientation relationship. The austenite $[100]_a$ direction is found to be parallel to the martensite $[110]_m$ direction in this case, confirming the origin of the sandwiched area as retained austenite.

- (2) In the BM2 sample, grown with a pulling rate of $7.7 \mu\text{m}\cdot\text{s}^{-1}$ and annealed at 1373K for 72h, the matrix is austenite. Besides the complicated dendritic γ' precipitates similar to the observations in Bg190 sample, some micron-sized precipitates formed in the matrix without, or with a single or three $(-111)_p$ twin planes parallel to the central axis. These precipitates with twinning structure have a specific orientation distribution due to the existence of the twin planes and the Kurdjumov-Sachs orientation relationship between precipitates and matrix. The growth of these kinds of precipitates can be explained by the Twin Plane Re-entrant Edge growth theory. No chemical gradient zone was observed across the interface of precipitates and austenite. The 3 D morphologies of the precipitates without twinning plane have a slab-like shape, while the precipitates with one twinning plane have a flat sheet-like shape revealed by Slice-and-View technique. The Lorentz microscopy study reveals that precipitates without twinning plane have a closure domain and the easy axis is parallel to the $[-11-1]$ at the room temperature. An in-situ cooling study of the matrix is also carried out. The austenite matrix has a 180° parallel domain, and the easy axis is parallel to $[100]$ or $[111]$.

Publications

Microstructure study of the precipitation behaviour in Co38Ni33Al29 ferromagnetic shape memory alloys, J.B. Lu, S. Sedlakova-Ignacova, R. Espinoza, H. Shi, J. Kopeček, P. Sittner, D. Schryvers, B. Bártová, to be published

Magnetic study of the precipitation behaviour in Co38Ni33Al29 ferromagnetic shape memory alloys, J.B. Lu, J. Kopeček, P. Sittner, D. Schryvers, to be published

Recent EM investigations on nano- and micro-defect structures in SMAs, D. Schryvers, S. Cao, S. Pourbabak, H. Shi, J.B. Lu, Journal of Alloys and Compounds (proc. ICOMAT 2011, 4-9/09/11, Osaka, Jpn). accepted

Microstructure and intergrowth of defects in coffin-shaped ZSM-5 zeolite crystals revealed by FIB-assisted HRTEM, JB Lu, D Schryvers, MJB Roeffaers, E Bartholomeeusen, B Sels, proc. emc2012, 16-21/09/12, Manchester, UK